



1 **Thermal Annealing of Implanted ^{252}Cf Fission-Tracks in Monazite**

2

3

Sean Jones, Andrew Gleadow, Barry Kohn

4

5

School of Earth Sciences, University of Melbourne, Victoria 3010, Australia

6

7

Correspondence: Sean Jones (seanj1@student.unimelb.edu.au)

8

9

Abstract

10

11

12

13

14

15

16

17

18

19

20

21

22

23

24

25

26

27

28

29

30

A series of isochronal heating experiments were performed to constrain monazite fission-track thermal annealing properties. ^{252}Cf fission-tracks were implanted into monazite crystals from the Devonian Harcourt Granodiorite (Victoria, Australia) on polished surfaces oriented parallel and perpendicular to (100) prismatic faces. Tracks were annealed over 1, 10, 100 and 1000 hour schedules at temperatures between 30°C and 400°C. Track lengths were measured on captured digital image stacks, and then converted to calculated mean lengths of equivalent confined fission tracks which progressively decreased with increasing temperature and time. Annealing is anisotropic, with tracks on surfaces perpendicular to the crystallographic c-axis consistently annealing faster than those on surfaces parallel to c. To investigate how the mean track lengths decreased as a function of annealing time and temperature, one parallel and two fanning models were fitted to the empirical dataset. The temperature limits of the monazite partial annealing zone (MPAZ) were defined as length reductions to 0.95 (lowest) and 0.5 (highest) for this study. Extrapolation of the laboratory experiments to geological timescales indicates that for a heating duration of 10^7 years, estimated temperature ranges of the MPAZ are -44 to 101°C for the parallel model and -71 to 143°C (both $\pm 6 - 21^\circ\text{C}$, 2 standard errors) for the best fitting linear fanning model ($T_0 = \infty$). If a monazite fission-track closure temperature is approximated as the mid-point of the MPAZ, these results, for tracks with similar mass and energy distributions to those involved in spontaneous fission of ^{238}U , are consistent with previously estimated closure temperatures (calculated from substantially higher energy particles) of $<50^\circ\text{C}$ and perhaps not much above ambient surface temperatures. Based on our findings we estimate that this closure temperature (T_c) for fission



31 tracks in monazite ranges between ~45 and 25°C over geological timescales of 10^6 – 10^7 years
32 making this system potentially useful as an ultra-low temperature thermochronometer.

33

34 **1. Introduction**

35 Fission track thermochronology is an analytical technique used to reconstruct the low-
36 temperature thermal history of rocks over geological time. Fission tracks form from the
37 spontaneous nuclear fission of ^{238}U , resulting in the accumulation of narrow damage trails in
38 uranium-bearing minerals such as apatite and zircon. The time since the fission tracks began
39 to accumulate may be calculated by measuring the spontaneous track density and uranium
40 concentration. If the host rock experienced elevated temperatures, the fission tracks that
41 have formed up to that point will progressively anneal and eventually disappear. Thermal
42 diffusion drives the annealing process, with the reduction in fission track density and confined
43 track length being a function of heating time and temperature in the host rock. From the
44 apparent age and track length distribution a quantitative analysis of the thermal history of
45 the host rock can be achieved. For fundamentals of the fission track technique, including
46 methodology and applications see Wagner and Van den Haute (1992) and Malusa and
47 Fitzgerald (2019).

48

49 The occurrence of monazite as an accessory mineral, along with the presence of significant
50 uranium (U) and thorium (Th) incorporated in its crystal lattice make it a useful mineral for
51 isotopic and chemical dating (e.g. Badr et al., 2010; Cenki-Tok et al., 2016; Tickyj et al., 2004).
52 In monazite, studies have mostly focused on the U-Th-Pb and (U-Th)/He systems but only
53 limited research has been carried out into the potential of the fission track system, mainly
54 due to technological limitations. Conventional fission track dating relies on thermal neutron
55 irradiation of samples to obtain an estimate of ^{238}U content via the formation of ^{235}U fission
56 tracks, usually captured in an adjacent external solid-state track detector such as mica. This
57 approach, however, has hindered the development of monazite fission track dating for a
58 number of reasons. Monazite is highly unsuitable for irradiation due to massive self-shielding
59 by thermal neutron capture from gadolinium (Gd), which may reach abundances in excess of
60 2 wt%. Gd has an extremely high thermal neutron capture cross-section of 48,890 barns,
61 averaged over its constituent isotopes, compared to 580 barns for ^{235}U fission (Gleadow et
62 al., 2004; Weise et al., 2009). An even more serious issue is that neutron capture by Gd



63 induces substantial nuclear heating in monazite during irradiation, which may be sufficient to
64 melt the grains and would certainly anneal any fission tracks produced.

65 These factors have also ruled out conventional annealing studies dependent on neutron-
66 induced ^{235}U fission tracks to assess the geological stability of fission tracks in this mineral.
67 Alternative thermal annealing experiments have been developed using implanted heavy ion
68 tracks (e.g. Weise et al., 2009; Ure, 2010), in place of ^{235}U induced fission tracks. These
69 methods, in combination with the use of Laser Ablation ICP Mass Spectrometry (LA-ICPMS)
70 or Electron Probe Microanalysis (EPMA) for determining U concentrations on individual
71 grains, provide alternatives to the traditional neutron-irradiation approach, thus allowing the
72 potential of monazite fission track dating to be assessed.

73

74 The first published study of fission track dating in monazite was by Shukoljukov and Komarov
75 (1970), who reported very young ages for two monazite samples from Kazakhstan. The
76 unexpectedly young results obtained were the first to suggest that fission tracks in monazite
77 anneal at relatively low temperatures (Shukoljukov and Komarov, 1970). Since this study, the
78 majority of reported monazite fission track studies have been in conference abstracts (e.g.
79 Fayon, 2011, Gleadow et al., 2004, and Shipley and Fayon, 2006). Gleadow et al. (2004)
80 reported preliminary results on several monazite samples revealing fission track ages
81 considerably younger than corresponding apatite fission track ages, further suggesting that
82 monazite fission tracks anneal at lower temperatures. This finding was later confirmed by
83 Shipley and Fayon (2006), who also suggested that annealing rates may vary as a function of
84 uranium concentration.

85

86 A comprehensive annealing study using 300MeV ^{86}Kr heavy ion tracks in monazite was
87 published by Weise et al. (2009). Three isochronal annealing sequences were carried out over
88 schedules of 1, 20 and 100 hr/s on crystals cut parallel to the (100) face. Adapting simplified
89 apatite annealing models and extrapolating the results to geological timescales they
90 estimated a closure temperature that “is in all likelihood $<50^\circ\text{C}$ and perhaps not much above
91 ambient”.

92

93 Ure (2010) carried out further thermal annealing experiments on monazite based on
94 implanted ^{252}Cf fission tracks. These were carried out on grains mounted parallel and



95 perpendicular to the crystallographic c-axis, with each orientation annealed for 20 minutes
96 and 1 hour at various temperatures. The results showed that on these short laboratory time
97 scales, ^{252}Cf tracks in monazite annealed at lower temperatures when compared to parallel
98 experiments on Durango Apatite. Further, it was concluded that monazite exhibits similar
99 anisotropic annealing properties to apatite in that tracks anneal faster perpendicular to the
100 c-axis compared to the c-axis parallel direction. All of these studies have suggested that fission
101 tracks in monazite have significant potential as a new ultra-low temperature
102 thermochronometer, but that further work is required to quantify the annealing kinetics.

103

104 Several studies have used heavy ion tracks as proxies for fission track annealing studies in
105 other minerals. Green et al. (1986) annealed 220-MeV Ni ion tracks in apatite to further
106 confirm that gaps in the etchability of highly annealed tracks delay the progress of the etchant
107 along the track length. Sandhu et al., (1990) implanted heavy ion tracks of various energies
108 (1.67 GeV Nb, 3.54 GeV Pb and 2.38 GeV U) in mica, apatite and zircon, and concluded that
109 the activation energies for annealing the different energy ion tracks were identical in the
110 same mineral. Furthermore, they found that in the same mineral, the activation energies for
111 annealing of tracks formed by ^{252}Cf fission fragments were also identical to those from the
112 heavy ion tracks. These studies have shown that the minimum energy required to initiate
113 annealing is largely independent of the nature and energy of the ion source and rather is a
114 property of the detector mineral (Sandhu et al., 1990). Because the mass and energy
115 distributions of both light and heavy fission fragments from ^{252}Cf are similar to those
116 produced by spontaneous fission of ^{238}U , the annealing properties of fission tracks from either
117 source in monazite should be similar (Fleischer et al., 1975).

118

119 In this study, implanted ^{252}Cf fission tracks are used to constrain the thermal annealing
120 properties of monazite using a modified etching protocol (Jones et al., 2019). The new
121 annealing experiments cover a wider time-temperature range than previously reported.
122 Three alternative kinetic models are then developed that describe the reduction of fission
123 track lengths as functions of time and temperature. Extrapolation of these models then allows
124 estimates to be made of the temperature range over which fission-track annealing occurs on
125 geological timescales.

126



127 **2. Experimental methods**

128 Monazite crystals used in the thermal annealing experiments were separated from the Late
129 Devonian Harcourt Granodiorite (Victoria, Australia). This is a high-K, calc-alkaline granite
130 dated by zircon U-Pb and $^{40}\text{Ar}/^{39}\text{Ar}$ geochronology to ~ 370 Ma (Clemens, 2018). Euhedral
131 monazite crystals range from $\sim 100 - 250$ μm in length and are classified as Ce dominant (see
132 Table 1).

133

134 **Table 1.** Average electron microprobe analyses of Harcourt Granodiorite monazite grains

Element	Mean Wt.%
SiO ₂	1.63 ± 0.04
P ₂ O ₅	27.37 ± 0.15
CaO	0.45 ± 0.02
Y ₂ O ₃	2.39 ± 0.05
La ₂ O ₃	14.13 ± 0.17
Ce ₂ O ₃	28.54 ± 0.26
Pr ₂ O ₃	4.45 ± 0.11
Nd ₂ O ₃	10.61 ± 0.13
Sm ₂ O ₃	1.80 ± 0.08
Gd ₂ O ₃	1.34 ± 0.08
ThO ₂	6.31 ± 0.11
UO ₂	0.50 ± 0.04
Sum Ox%	99.52

Measurements ($\pm 2\sigma$ error) on 81 grains made with a Cameca SX50 electron microprobe using a 10 μm beam width, 50 KeV beam current, 25 KV accelerating voltage and take off angle of 40°.

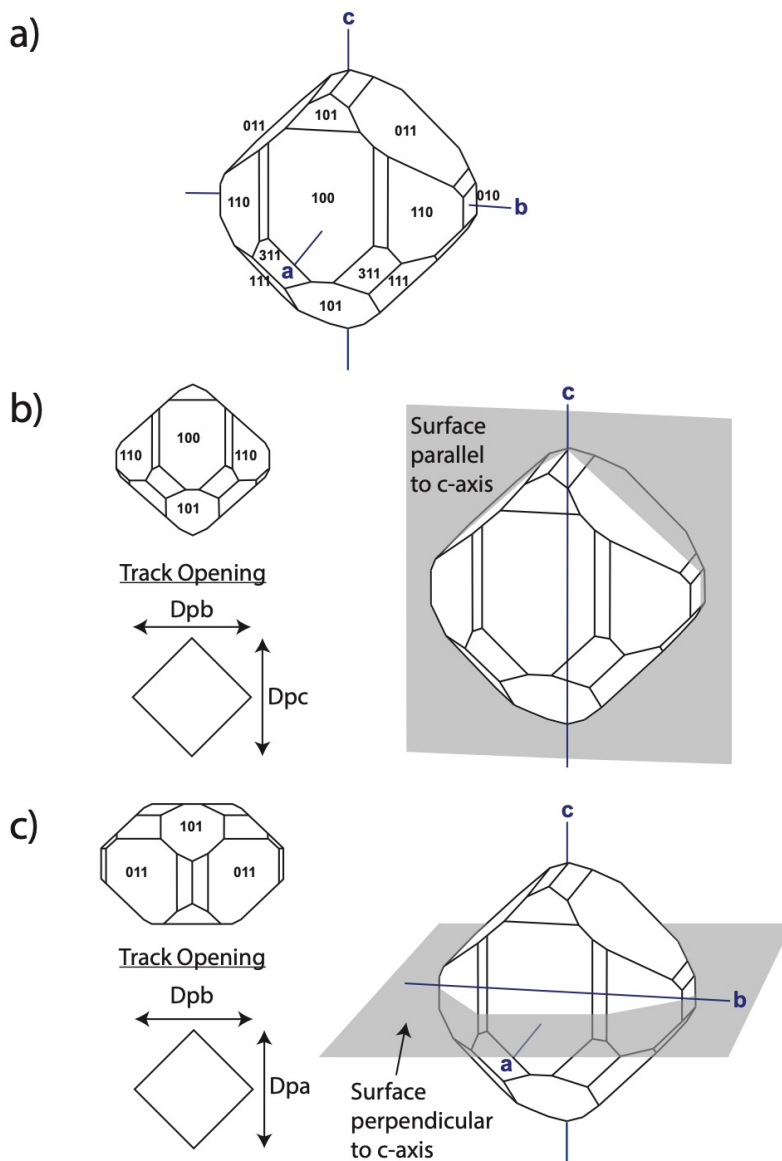
135

136

137 ^{252}Cf fission track implantation, measurements and equivalent confined fission track
138 calculations in this study essentially followed the procedure of Ure (2010). Fifty-five monazite
139 crystals per sample were attached to double-sided tape on a Teflon block. Then using
140 tweezers under a stereoscopic microscope, grains were carefully oriented parallel (//) and
141 perpendicular (\perp) to the crystallographic c-axis (Figure 1), followed by mounting in cold
142 setting *Struers* Epofix epoxy. For each annealing experiment, two sample mounts were made,
143 one with grains orientated parallel and another perpendicular to the c-axis. Each sample
144 mount was then pre-ground using a *Struers* MD-Piano 1200 grinding disc and final polishing
145 with 6, 3, 1 and 0.25 μm diamond pastes. Polished grain mounts were then exposed to
146 collimated fission fragments approximately 2 cm from a thin 4mm diameter ^{252}Cf source
147 under vacuum for 7 hours to implant a density of $\sim 5 \times 10^6$ tracks/cm². Tracks were implanted
148 at an angle of approximately 30° to the polished surface which had been shown to be optimal
149 for measurement in previous experiments (Ure, 2010).



150



151

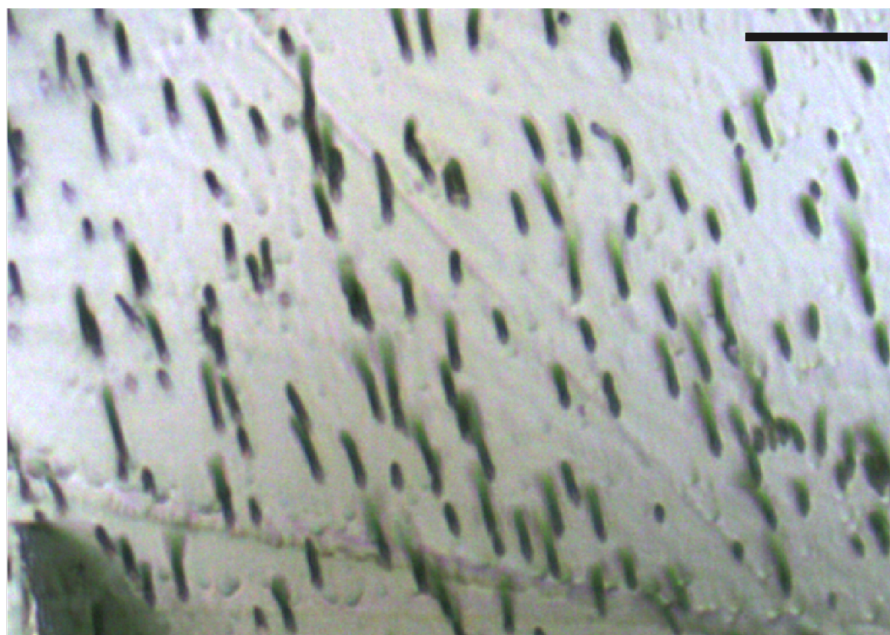
152 **Figure 1.** (a) Typical monazite crystal with Miller Indices and crystallographic axes. (b) Crystal plane for tracks
 153 implanted on surfaces parallel to the crystallographic c-axis. The shape of the track opening on the etched
 154 surface is a rhombus. Dpb represents diameter of etch pit parallel to b-axis and Dpc is defined as the diameter
 155 of etch pit parallel to c-axis, equivalent to the parameters Dper and Dpar respectively in uniaxial minerals such
 156 as apatite. (c) Crystal plane for tracks implanted perpendicular to c-axis. Track etch pits also tend to be diamond
 157 in shape. Dpa represents diameter of track opening parallel to a-axis. Models from Mindat.org.



158

159 Following track implantation, grains were removed from the mount by dissolving the epoxy
160 mount in commercial paint-stripper. The loose grains were then annealed in aluminum tubes
161 in a *Ratek Digital* Dry Block Heater over 1-, 10-, 100- and 1000-hour schedules at
162 temperatures between 30°C - 400°C. The block heater was covered by a ceramic foam block
163 for insulation through which a probe could be inserted to monitor temperatures.
164 Temperature uncertainty is estimated to be $\pm 2^\circ\text{C}$. Once each annealing experiment was
165 completed, the grains were removed from the block heater and re-mounted, polished face
166 down, on double-sided tape before re-embedding in cold setting *Epofix* epoxy. Etching of each
167 sample mount was then performed using 6M HCl for 75 minutes at 90°C (Jones et al., 2019).
168 An example of well-etched ^{252}Cf fission tracks in this monazite is shown in Figure 2.

169



170

171 **Figure 2.** Implanted and well-etched ^{252}Cf fission tracks in Harcourt Granodiorite monazite. Enlarged image taken
172 with a 100x dry objective, scale bar is 10 μm .

173

174 Digital images of all monazite grains in each mount were captured in reflected and
175 transmitted light using a 100x dry objective on a *Zeiss Axio Imager M1m* motorized
176 microscope fitted with a *PI* piezo-motor scanning stage and an *IDS μEye 4* Megapixel USB 3



177 CMOS digital camera. This was interfaced to a control PC using *Trackworks* software (Gleadow
178 et al., 2009; 2019). The true 3D lengths of the etched ^{252}Cf semi-tracks were then measured
179 from the captured image stacks on a separate computer using *FastTracks* software (Gleadow
180 et al., 2009; 2019) until a maximum of 500 tracks per sample mount were attained, thus
181 totaling 1000 tracks per annealing experiment (500 on the c-axis parallel and 500 on the c-
182 axis perpendicular surfaces). Track length measurements were made using both reflected and
183 transmitted light images and typically measured over ~ 30 grains. The surface reflected light
184 image was used to manually determine the center of the implanted ^{252}Cf semi-track etch pit,
185 and the transmitted light stack for determining the position of the track termination by
186 scrolling down through the image stack to the last image plane where it appeared clearly in
187 focus. *FastTracks* automatically calculates true track lengths, correcting the vertical focus
188 depth for the refractive index of monazite, taken to be 1.794.

189

190 The equivalent confined track length (l) was then calculated based on a correction for the
191 small amount of surface lowering during track etching. This surface lowering during etching
192 on different planes was estimated from diameters of the track etch pits in different directions.
193 In uniaxial minerals, such as apatite and zircon, the dimensions of track etch pits are
194 satisfactorily described by the parameters D_{par} and D_{per} (track diameters parallel and
195 perpendicular respectively to the c-axis, Donelick et al., 2005). However for monoclinic
196 minerals, such as monazite, the situation is more complex, and we extend this terminology as
197 shown in Figure 1 with three track diameter measurements, D_{pa} (diameter parallel to the a-
198 axis), D_{pb} (parallel to b) and D_{pc} (parallel to c), the latter being equivalent to D_{par} in apatite
199 and zircon. The track etch pits in monazite are rhombic in shape and in practice these three
200 diameter measurements are very similar to each other, so the differences are not critical
201 (Table 2).

202

203



204 **Table 2.** Average diameters of implanted ^{252}Cf fission track openings on both parallel and perpendicular surfaces
 205 for each annealing schedule.

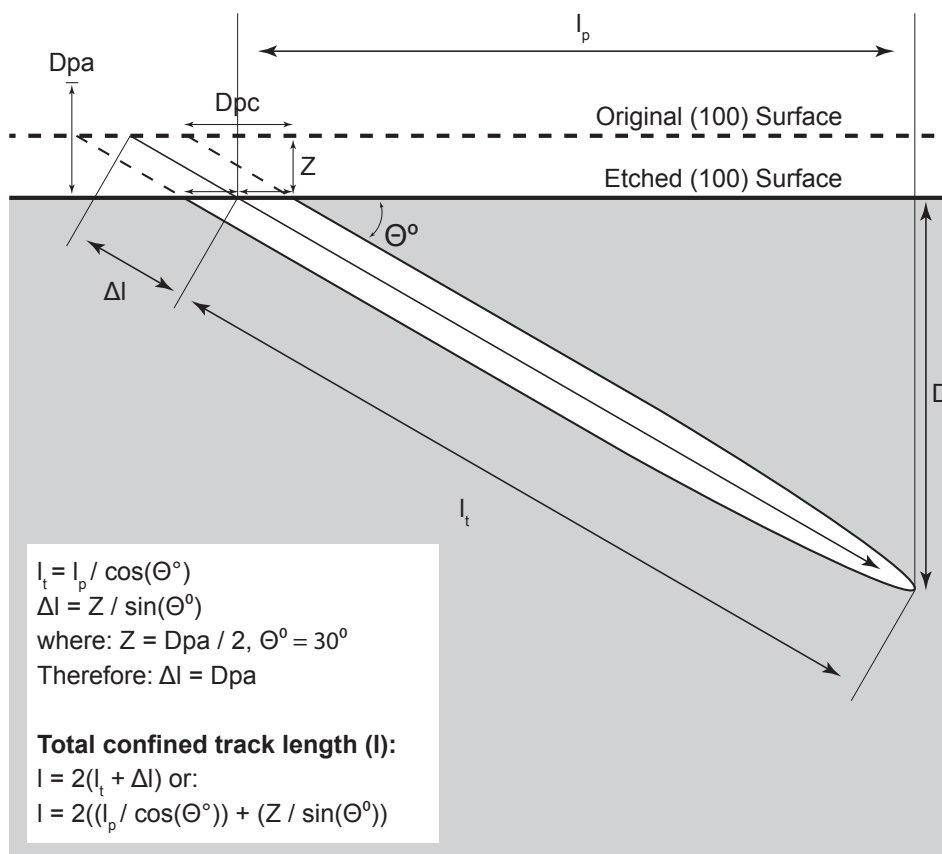
	Dpa (μm)	Dpb (μm)	Dpc (μm)
Surfaces // c-axis			
1 Hour	-	0.62	0.61
10 Hours	-	0.64	0.60
100 Hours	-	0.62	0.63
1000 Hours	-	0.61	0.60
Surfaces \perp c-axis			
1 Hour	0.62	0.61	-
10 Hours	0.62	0.63	-
100 Hours	0.63	0.64	-
1000 Hours	0.63	0.64	-
Average	0.63	0.62	0.61

206

207

208 The track diameter measurements, representing the rate of etching from a point source in
 209 different crystallographic orientations, may be used to estimate the rate of surface lowering
 210 on different surfaces. For (100) surfaces (i.e. parallel to both b- and c-axes), the amount of
 211 surface etching was estimated using measurements of the track width parameter Dpa,
 212 measured on the surface normal to the c-axis (approximately parallel to the a- and b-axes).
 213 Diameter measurements were made for approximately 250 tracks for both surface
 214 orientations in each sample. The amount of surface etching on (100) was approximated by
 215 half the mean Dpa measurement for each sample (Ure, 2010). Knowing the track implantation
 216 angle (30°), allows for the length of the lost portion of the implanted semi-tracks to be
 217 calculated and added to the total track length (Ure, 2010) as illustrated in Figure 3. The
 218 equivalent confined fission track length is then obtained by doubling the corrected mean
 219 semi-track length. For surfaces cut perpendicular to the c-axis (approximately (001)), the
 220 relevant measurement for the surface lowering correction is the half the mean Dpc measured
 221 on the (100) surfaces.

222



223

224 **Figure 3.** Illustration of the measurements and calculations required to correct semi-track lengths for surface
 225 etching on a (100) face (ie parallel to b and c). Bulk etching removes the original surface by approximately half
 226 the width of the etch pit diameter parallel to the a-axis (Dpa) measured on the $\sim(001)$ face (modified from Ure
 227 2010).

228

229 **3. Results**

230 Table 3 and Figure 4 present the track length measurements from the isochronal annealing
 231 experiments in Harcourt Granodiorite monazite. All length measurements are presented as
 232 mean lengths of equivalent confined fission tracks calculated according to the geometry in
 233 Figure 3 and duplicated on surfaces orientated parallel and perpendicular to the
 234 crystallographic c-axis. The annealing schedules are presented as 1, 10, 100 and 1000 hours
 235 between temperatures of 30°C - 400°C.

236



237 Unannealed fission track lengths for all control samples range from 10.12 ± 0.06 – $11.23 \pm$
238 $0.08 \mu\text{m}$, averaging $10.60 \pm 0.19 \mu\text{m}$. These vary by considerably more than the analytical
239 uncertainty and possible reasons for this are considered below. Across all annealing
240 experiments, mean lengths become progressively shorter, down to a minimum measured
241 length of $4.88 \mu\text{m}$ (10 hours, 300°C , perpendicular c-axis). Note that for all the annealed
242 samples tracks etched on surfaces perpendicular to the crystallographic c-axis are always
243 shorter than the average length of tracks orientated on surfaces parallel to c. However, the
244 same is not true for all of the control measurements.

245

246 Track length reduction normalized to the mean length for the unannealed control samples
247 ($10.60 \mu\text{m}$) are also presented in Table 3. Normalized lengths start at 1 (control sample),
248 reducing to ~ 0.5 before dropping abruptly to zero by the next heating step. The shortest mean
249 track lengths were seen in the 10-hour experiments, where l/l_0 decreased to values of 0.502
250 and 0.460 (300°C , parallel and perpendicular surfaces, respectively).

251

252 **Table 3.** Isochronal laboratory annealing data for ^{252}Cf tracks in the Harcourt Granodiorite monazite (1σ errors).



Annealing Time	Annealing Temp (°C)	Surface Orientation	²⁵² Cf Track Length (µm)*	Z (µm)	Calculated Track Length (µm)**	I/I_0 (r)	No. of Tracks
Control	~20	// c-axis	4.60 ± 0.84	0.31	10.42 ± 0.08	1	500
1 Hour	50	// c-axis	4.29 ± 0.82	0.30	9.78 ± 0.07	0.923 ± 0.010	500
1 Hour	100	// c-axis	4.05 ± 0.69	0.32	9.36 ± 0.06	0.883 ± 0.009	500
1 Hour	200	// c-axis	3.34 ± 0.73	0.34	8.02 ± 0.07	0.757 ± 0.009	500
1 Hour	300	// c-axis	2.90 ± 0.73	0.31	7.02 ± 0.06	0.662 ± 0.008	500
1 Hour	320	// c-axis	2.60 ± 0.82	0.31	6.42 ± 0.07	0.606 ± 0.008	500
1 Hour	400	// c-axis	0	0	0	0	0
Control	~20	⊥ c-axis	5.00 ± 0.88	0.31	11.23 ± 0.08	1	500
1 Hour	50	⊥ c-axis	4.27 ± 0.82	0.30	9.74 ± 0.07	0.919 ± 0.009	500
1 Hour	100	⊥ c-axis	4.01 ± 0.72	0.31	9.24 ± 0.06	0.872 ± 0.008	500
1 Hour	200	⊥ c-axis	3.25 ± 0.70	0.32	7.76 ± 0.06	0.732 ± 0.007	500
1 Hour	300	⊥ c-axis	2.60 ± 0.74	0.32	6.48 ± 0.06	0.611 ± 0.007	500
1 Hour	320	⊥ c-axis	2.44 ± 0.73	0.33	6.18 ± 0.07	0.583 ± 0.007	500
1 Hour	400	⊥ c-axis	0	0	0	0	0
Control	~20	// c-axis	4.82 ± 0.57	0.32	10.90 ± 0.05	1	500
10 Hours	50	// c-axis	4.20 ± 0.71	0.30	9.60 ± 0.06	0.906 ± 0.007	500
10 Hours	100	// c-axis	3.82 ± 0.62	0.33	8.94 ± 0.06	0.843 ± 0.007	500
10 Hours	150	// c-axis	3.43 ± 0.64	0.34	8.22 ± 0.06	0.775 ± 0.007	500
10 Hours	200	// c-axis	3.17 ± 0.60	0.30	7.54 ± 0.06	0.711 ± 0.006	500
10 Hours	250	// c-axis	2.77 ± 0.69	0.34	6.88 ± 0.06	0.649 ± 0.006	500
10 Hours	300	// c-axis	2.03 ± 0.72	0.32	5.32 ± 0.06	0.502 ± 0.006	500
10 Hours	350	// c-axis	0	0	0	0	0
Control	~20	⊥ c-axis	4.65 ± 0.53	0.33	10.62 ± 0.05	1	500
10 Hours	50	⊥ c-axis	4.15 ± 0.69	0.31	9.54 ± 0.06	0.900 ± 0.007	500
10 Hours	100	⊥ c-axis	3.81 ± 0.54	0.30	8.82 ± 0.05	0.832 ± 0.006	500
10 Hours	150	⊥ c-axis	3.40 ± 0.68	0.30	8.00 ± 0.06	0.755 ± 0.007	500
10 Hours	200	⊥ c-axis	3.09 ± 0.66	0.30	7.38 ± 0.06	0.696 ± 0.007	500
10 Hours	250	⊥ c-axis	2.63 ± 0.66	0.33	6.56 ± 0.06	0.619 ± 0.006	500
10 Hours	300	⊥ c-axis	1.81 ± 0.71	0.32	4.88 ± 0.06	0.460 ± 0.006	500
10 Hours	350	⊥ c-axis	0	0	0	0	0
Control	~20	// c-axis	4.85 ± 0.75	0.30	10.90 ± 0.07	1	500
100 Hours	30	// c-axis	4.46 ± 0.90	0.30	10.12 ± 0.08	0.955 ± 0.009	500
100 Hours	50	// c-axis	4.19 ± 0.94	0.31	9.62 ± 0.08	0.908 ± 0.009	500
100 Hours	100	// c-axis	3.75 ± 0.68	0.30	8.70 ± 0.06	0.821 ± 0.008	500
100 Hours	150	// c-axis	3.32 ± 0.80	0.34	7.98 ± 0.07	0.753 ± 0.008	500
100 Hours	200	// c-axis	3.04 ± 0.70	0.34	7.44 ± 0.06	0.702 ± 0.007	500
100 Hours	250	// c-axis	2.51 ± 0.73	0.32	6.28 ± 0.07	0.592 ± 0.007	500
100 Hours	300	// c-axis	0	0	0	0	0
100 Hours	350	// c-axis	0	0	0	0	0
Control	~20	⊥ c-axis	4.50 ± 0.76	0.30	10.20 ± 0.07	1	500
100 Hours	30	⊥ c-axis	4.26 ± 0.84	0.32	9.80 ± 0.08	0.925 ± 0.010	500
100 Hours	50	⊥ c-axis	4.05 ± 0.83	0.33	9.42 ± 0.07	0.889 ± 0.009	500
100 Hours	100	⊥ c-axis	3.65 ± 0.63	0.31	8.54 ± 0.06	0.806 ± 0.008	500
100 Hours	150	⊥ c-axis	3.31 ± 0.74	0.32	7.90 ± 0.07	0.745 ± 0.008	500
100 Hours	200	⊥ c-axis	3.01 ± 0.69	0.32	7.28 ± 0.06	0.687 ± 0.008	499
100 Hours	250	⊥ c-axis	2.49 ± 0.53	0.32	6.24 ± 0.05	0.589 ± 0.006	500
100 Hours	300	⊥ c-axis	0	0	0	0	0
100 Hours	350	⊥ c-axis	0	0	0	0	0
Control	~20	// c-axis	4.46 ± 0.64	0.30	10.12 ± 0.06	1	500
1000 Hours	50	// c-axis	4.03 ± 0.60	0.30	9.26 ± 0.06	0.874 ± 0.008	500
1000 Hours	150	// c-axis	3.18 ± 0.54	0.31	7.60 ± 0.05	0.717 ± 0.007	500
1000 Hours	200	// c-axis	3.04 ± 0.74	0.30	7.28 ± 0.07	0.687 ± 0.007	500
1000 Hours	250	// c-axis	2.60 ± 0.96	0.31	6.42 ± 0.09	0.606 ± 0.007	500
1000 Hours	275	// c-axis	0	0	0	0	0
Control	~20	⊥ c-axis	4.58 ± 0.65	0.31	10.40 ± 0.06	1	500
1000 Hours	50	⊥ c-axis	3.99 ± 0.60	0.30	9.18 ± 0.06	0.866 ± 0.008	500
1000 Hours	150	⊥ c-axis	3.15 ± 0.52	0.31	7.56 ± 0.05	0.713 ± 0.006	500
1000 Hours	200	⊥ c-axis	2.79 ± 0.59	0.33	6.88 ± 0.05	0.649 ± 0.006	500
1000 Hours	250	⊥ c-axis	2.02 ± 1.08	0.33	5.36 ± 0.16	0.506 ± 0.008	187
1000 Hours	275	⊥ c-axis	0	0	0	0	0

* ± sd, ** ± se

Z is the amount of surface lowering due to bulk etching

I/I_0 (r) has been normalized to average control sample of 10.60 µm



254

255 **4. Discussion**

256 The average track length for the unannealed control samples across all analyses is $10.60 \pm$
257 $0.19 \mu\text{m}$ which is slightly shorter but within error of the $11.30 \pm 0.36 \mu\text{m}$ mean length reported
258 by Ure (2010) for a smaller number of tracks in a different monazite of unknown composition.
259 Weise et al. (2009) calculated a mean range $8.30 \pm 0.62 \mu\text{m}$ for a heavy fission fragment and
260 $10.80 \pm 0.52 \mu\text{m}$ for a light fission fragment for ^{235}U fission in monazite. This combines to give
261 a total latent track length of $\sim 19 \mu\text{m}$. However, it has long been known (e.g. Fleischer et al.,
262 1975) that the lengths of etched fission tracks are significantly shorter than the total range of
263 the fission fragments due to a 'length deficit' of unetchable radiation damage towards the
264 end of the track. Weise et al. (2009) calculated the length deficit for a unannealed confined
265 fission track in monazite to be $6\text{--}7 \mu\text{m}$, making the etchable length for induced ^{235}U fission
266 tracks $\sim 12\text{--}13 \mu\text{m}$. Our measurements for the unannealed control samples are on average $\sim 1\text{--}$
267 $2 \mu\text{m}$ shorter than these estimates, suggesting that the length deficit may be closer to $8 \mu\text{m}$
268 ($\sim 4 \mu\text{m}$ at each end) at least for the ^{252}Cf tracks used here. The mean track lengths reported
269 here are also broadly consistent with measured lengths of spontaneous ^{238}U confined tracks,
270 reported to be $\sim 10 \mu\text{m}$ (Weise et al., 2009).

271

272 There is a difference of $1.11 \mu\text{m}$ between the longest and shortest mean track lengths in
273 control samples across the experiments. This is substantial and significantly greater than the
274 measurement uncertainty. It is known that newly produced fission tracks in apatite undergo
275 rapid annealing at ambient temperatures (Donelick et al., 1990) from the moment the track
276 is formed in the crystal lattice until the track is etched. It was not clear whether this was due
277 to short-term thermal annealing or some non-thermal annealing mechanism. Belton (2006)
278 and Tamer and Ketcham (2020) also found similar effects in a series of ambient temperature
279 annealing experiments on freshly induced ^{235}U fission tracks in various apatites. The results
280 showed the tracks reduced in length by $0.32\text{--}0.70 \mu\text{m}$ between 39 seconds and 1.88 days
281 after irradiation and continued to shorten measurably over decades. While the exact amount
282 of time between ^{252}Cf track implantation and etching for each individual control sample was
283 not recorded in this study, the considerable length differences in the control samples suggest



284 that ambient temperature annealing may also occur in monazite, and probably to an even
285 greater degree than in apatite.

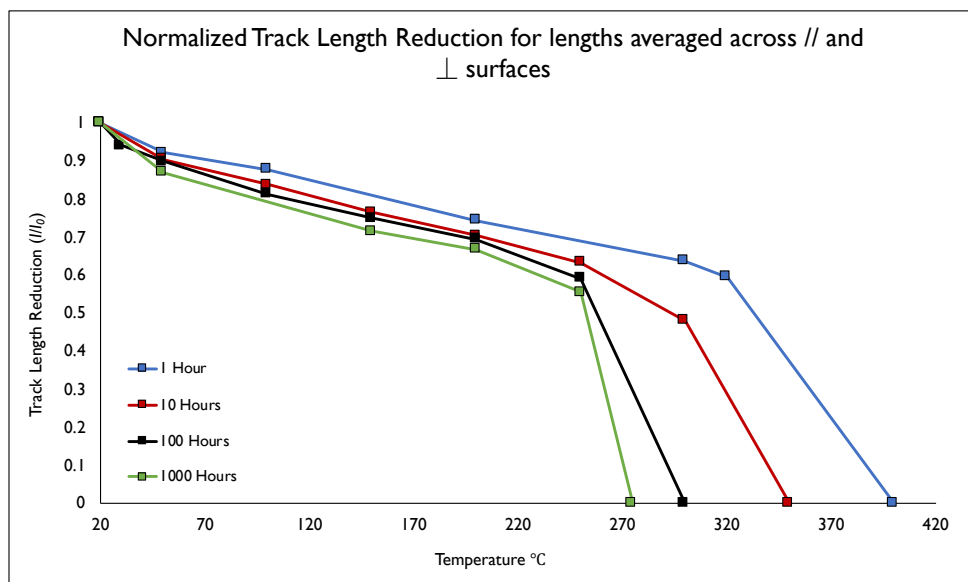
286

287 Differing degrees of ambient temperature annealing may also be the reason why mean track
288 lengths in monazite control samples cut perpendicular to the c-axis were not always shorter
289 than in those parallel to the c-axis, as was invariably the case for all experiments at higher
290 temperatures. Further, Figure 4 shows that for all the isochronal experiments, the annealing
291 curves exhibit an initial length reduction of ~5-10% before the 50°C annealing step, a feature
292 not observed in annealing experiments in other minerals. This may be due to the mean track
293 length for the control samples not having reached a stable value at ambient temperature
294 prior to the thermal annealing experiments.

295

296 Importantly, over the temperature range studied, no conditions have been identified where
297 the tracks are totally stable (Figure 4), even for experiments conducted at 30°C. Figure 2 also
298 shows that there is a gradual reduction in l/l_0 with temperature, followed by accelerated
299 reduction from ~0.580 to zero. For this reason, values of $l/l_0 < \sim 0.5$ are rarely encountered,
300 with only two slightly lower values (0.460 and 0.488) being observed amongst all 52
301 experiments. This is a similar behaviour to that seen in apatite and zircon (e.g. Green et al.,
302 1986; Yamada et al., 1995). Relatively less difference was observed between the averaged
303 track length reduction of the 100- and 1000- hour schedules compared to the shorter
304 annealing times.

305



306

307 **Figure 4.** Track length reduction (l/l_0) against temperature for calculated equivalent confined fission tracks in
308 Harcourt Granodiorite monazite. The track length reduction values are averaged across both parallel ($//$) and
309 perpendicular (\perp) surfaces with the normalized track length (l/l_0) values being calculated from the average length
310 of the unannealed control samples ($10.60 \mu\text{m}$).

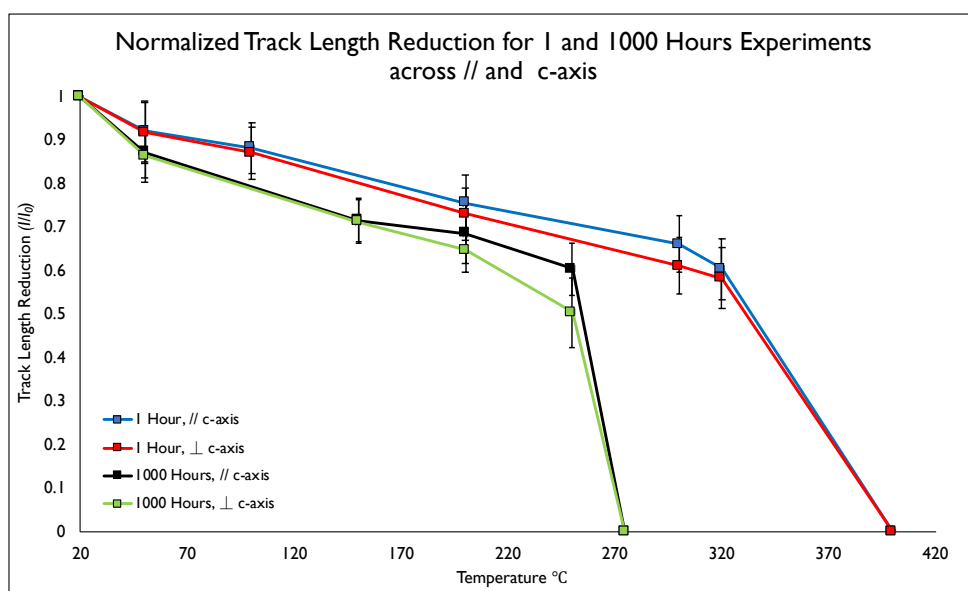
311

312 In all annealed samples, the mean equivalent confined track length was always less than that
313 for the unannealed control samples. As annealing progresses, the mean track lengths are
314 reduced, and become consistently anisotropic with crystallographic orientation, although the
315 differences are small and all within errors. Tracks implanted at 30° dip to polished surfaces
316 oriented perpendicular to the crystallographic c-axis always have shorter mean track lengths
317 than those at 30° to the c-axis parallel surfaces. On both these surface orientations the dips
318 were constant but there was limited control on the azimuth orientations of the collimated
319 tracks, so the exact relationship to crystallographic orientation is not clear. However, the
320 distribution of track orientations will cover a different range on the two surfaces so that
321 anisotropy of annealing can clearly be detected. As annealing progresses, the amount of
322 anisotropy generally increases across all annealing schedules for the two surface orientations
323 with the exception of 100 hours. That is, tracks on surfaces orientated perpendicular to the
324 crystallographic c-axis anneal faster with increasing temperature. Anisotropy is still present
325 in the 100-hour schedule, but no clear increase in the difference between calculated confined
326 track lengths is apparent for the two differently oriented surface planes. Anisotropy is



327 greatest in the 1000 hours, 250°C experiments, where there is a ~1.06 μm difference between
328 the two surface orientations (Figure 5). This is possibly due to only 187 semi-track lengths
329 being measured in the c-axis perpendicular aliquot (as most were completely annealed)
330 compared to 500 in the parallel aliquot.

331



332

333 **Figure 5.** Track length reduction (l/l_0) against temperature for calculated equivalent confined fission tracks for 1
334 and 1000 hour experiments for both surface orientations. The normalized track length (l/l_0) values are calculated
335 from the average length of the control samples (10.60 μm). Error bars refers to 1σ errors.

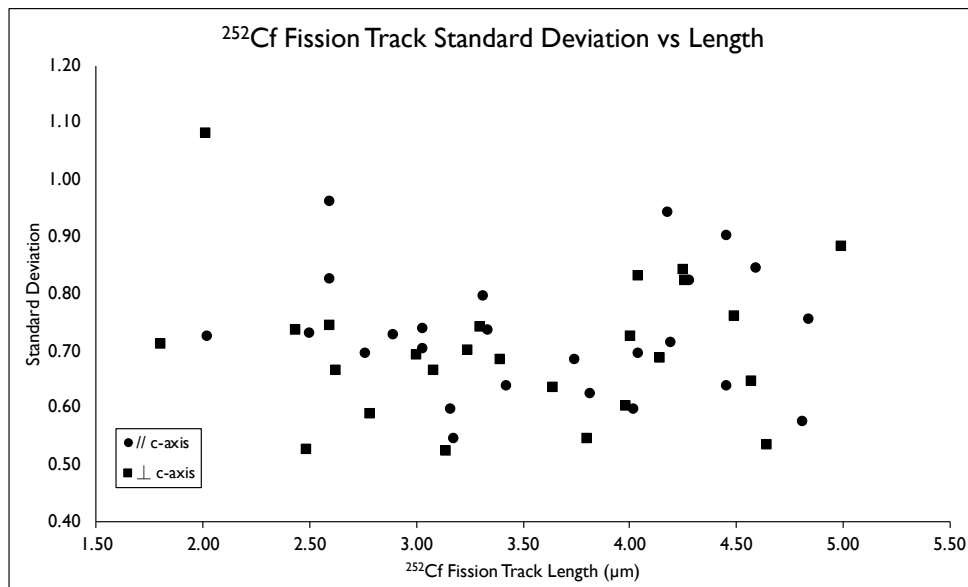
336

337 Figure 6 shows the relationship between the standard deviation and mean track length for
338 the length distributions of single fission fragment ^{252}Cf tracks. The results vary between 0.52
339 and 1.08 μm and are mostly consistent with a mean of 0.71 μm but with considerable scatter.
340 The results suggest an increase in standard deviation at short mean lengths, as is observed
341 for confined track length measurements in apatite during annealing (e.g. Green et al., 1986,
342 Fig 3) because of increasing anisotropy. For monazite, the amount of anisotropy also appears
343 to increase as the mean track length decreases giving an increase in dispersion of individual
344 track lengths, and hence standard deviation. The most extreme annealing observed is for the
345 1000 Hours, 250°C experiment, with a standard deviation of 1.08 μm, which shows the
346 greatest degree of anisotropy.



347

348



349

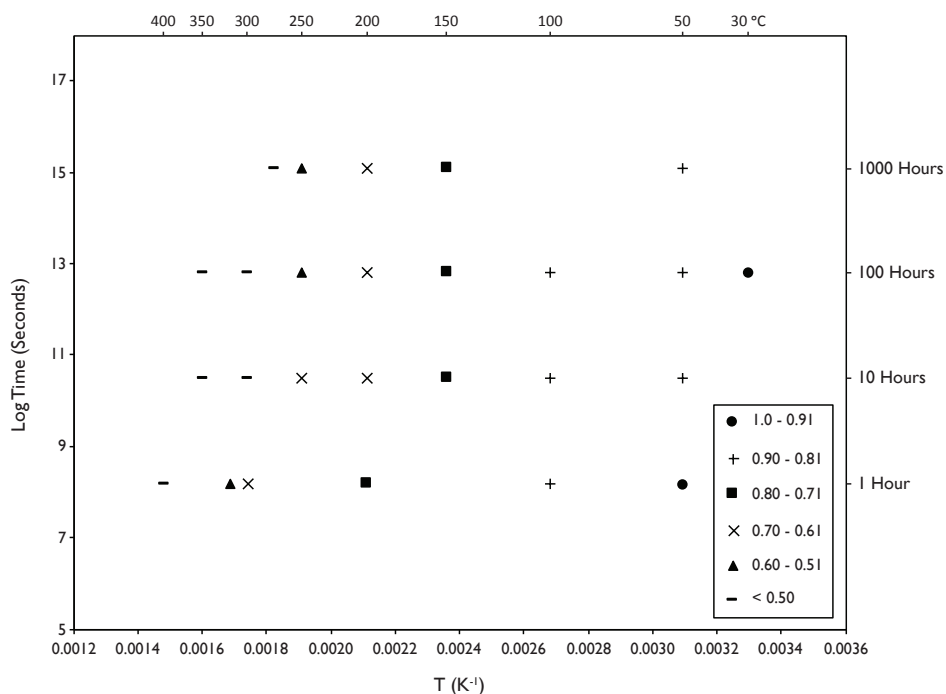
350 **Figure 6.** Standard deviation of ^{252}Cf fission-track length distributions plotted against their average track lengths
351 for both parallel and perpendicular surfaces across all experiments.

352

353 **5. The Arrhenius Plot**

354 Results of the Harcourt Grandiorite monazite annealing experiments are shown on an
355 Arrhenius plot of log time versus inverse absolute temperature in Figure 7. Results are
356 averaged across both surface orientations, and the normalized track length ($r=l/l_0$) values are
357 calculated relative to the average length of the unannealed control samples ($l_0 = 10.60 \mu\text{m}$).
358 In the plot, normalized track length values in a particular range are represented by the same
359 symbol and exhibit linear trends with positive correlation. To extrapolate laboratory
360 annealing results in Arrhenius plots to geological timescales, three types of model fitting have
361 traditionally been used to determine a functional form of the fission track annealing kinetics,
362 i.e. the 'parallel model' and two variations of the 'fanning model' (Laslett et al., 1987).

363



364

365 **Figure 7.** Arrhenius plot of experimental data using calculated equivalent confined fission track lengths in
 366 Harcourt Granodiorite monazite. Each point represents two annealing experiments that have been averaged
 367 across both orientations (parallel and perpendicular to c-axis). Different degrees of track length reduction (r) are
 368 shown by different symbols. Inverse absolute temperature in Kelvins shown on the x-axis and corresponding
 369 temperatures in °C along the top.

370

371 **5.1 Parallel Linear Model**

372 As a starting point, the annealing data of this study will be tested with the ‘parallel model’
 373 that has straight line contours (Laslett et al., 1987):

374

$$375 \quad \ln(t) = A(r) + B/T \quad (1)$$

376

377 Where t = annealing time; T = annealing temperature (K); $A(r)$ = intercept of the lines (at $1/T$
 378 = 0), which is a function of the most reliable values of normalized mean length r ; and B is the
 379 slope, which is a constant for all degrees of annealing. The intercept $A(r)$ is subject to the
 380 following constraints: (1) $A(r)$ decreases monotonically with increasing r ; and (2) $A(r = 1) \rightarrow$



381 $-\infty$ when $t \rightarrow 0$, $T \rightarrow 0$. It should be noted that $r = 0$ for finite values of t and T provided they
382 are large enough, in practice.

383 The fully parameterized parallel model has the form:

384

$$\begin{aligned} 385 \quad r &= c_1 + c_2 A(r) + \varepsilon \\ 386 \quad &= c_1 + c_2 [\ln(t) - B/T] + \varepsilon \end{aligned} \quad (2)$$

387 or

$$388 \quad g(r; a, b) = C_0 + C_1 \ln(t) + C_2/T + \varepsilon \quad (3)$$

389

390 Where $C_0 = c_1$; $C_1 = c_2$; $C_2 = -c_2 B$; $g(r; a, b)$ is a transform containing r and two parameters a
391 and b ; and ε represents errors or residuals. ε is assumed to be normally distributed with mean
392 $\mu = 0$ and constant variance σ^2 . This assumption can be checked by residual plot for the model
393 in Figure 9. A single Box-Cox transformation was adopted and was found to be better suited
394 to the data than the double Box-Cox (Box and Cox, 1964):

395

$$396 \quad g(r; a, b) = [\{ (1 - r^b) / b \}^a - 1] / a \quad (4)$$

397

398 In the model of Eq. 3, parameters and uncertainties (standard error) were evaluated for the
399 data sets in Table 4 as follows:

400

$$\begin{aligned} 401 \quad a &= 1, & b &= 3.72 \\ 402 \quad C_0 &= -0.440275 \pm 0.034626, & C_1 &= -0.019504 \pm 0.002284 \end{aligned}$$

403

404 and

405

$$406 \quad C_2 = 437.315478 \pm 10.901345$$

407

408 **5.2 Fanning Linear Model**

409 The fanning Arrhenius plot of Laslett et al. (1987) has slopes of contour lines that change with
410 a variation of activation energy E with the degree of annealing. In this case, Eq. 1 becomes:

411



412 $\ln(t) = A(r) + B(r) / T$ (5)

413

414 where both slope $B(r)$ and intercept $A(r)$ are a function of r . A first order assumption of this
415 equation is that $A(r)$ is a negative linear function of $B(r)$:

416

417 $A(r) = c_3 - c_4 B(r)$ (6)

418

419 where c_3 and c_4 are constants, by analogy with the ‘compensation law’ for diffusion (e.g., Hart,
420 1981). This causes the contours to fade and meet at a single point on the Arrhenius plot.

421 Combining Eqs. 4 and 5 becomes:

422

423 $\ln(t) = A^* + B(r) [(1/T) - (1/T_0)]$ (7)

424

425 where $A^* = c_3$; and $1/T_0 = c_4$. T_0 is known as the “critical temperature”, which is the
426 temperature of the ‘cross-over point’ of the fading contours (e.g. Crowley et al., 1991). Solving
427 Eq. 6 for $B(r)$ gives:

428

429 $B(r) = (\ln(t) - A^*) / [(1/T) - (1/T_0)]$ (8)

430

431 Constraints for slope $B(r)$ are: (1) $B(r)$ decreases monotonically with increasing r ; and (2) $B(r =$
432 $1) \rightarrow 0$ when $\ln(t) \rightarrow A^*$, $T \rightarrow 0$. The fully parameterized model is given as:

433

434 $r = c_1 + c_2 B(r) = c_1 + c_2 \{[\ln(t) - A^*] / [(1/T) - (1/T_0)]\} + \varepsilon$ (9)

435

436 or

437

438 $r = C_0 + (C_1 \ln(t) + C_2) / [(1/T) - C_3] + \varepsilon$ (10)

439

440 where $C_0 = c_1$; $C_1 = c_2$; $C_2 = -c_2 A^*$; and $C_3 = 1/T_0$.

441



442 When $C_3 = 0$, this assumes an infinite critical temperature (i.e., $T_0 = \infty$). The equation can be
443 rearranged to:

444

$$445 \quad r = C_0 + C_1 T \ln t + C_2 T + \varepsilon \quad (11)$$

446

447 The number of parameters is reduced from four to three, simplifying the equation. The
448 parameters and uncertainties (standard error) for the models in Eq. 10 were calculated as
449 follows:

$$450 \quad C_0 = 1.374 \pm 0.02698, \quad C_1 = -0.001105 \pm 0.00007301$$

451

452 and

453

$$454 \quad C_2 = -0.00002979 \pm 0.000004959$$

455

456 In the case where $T_0 \neq \infty$, Eq. 9 was adopted for the fitting calculation. The parameters and
457 uncertainties were evaluated as follows:

458

$$459 \quad C_0 = 1.227 \pm 0.09638, \quad C_1 = -0.00002418 \pm 0.000005221,$$

460

$$461 \quad C_2 = -0.0005491 \pm 0.0003005$$

462

463 and

464

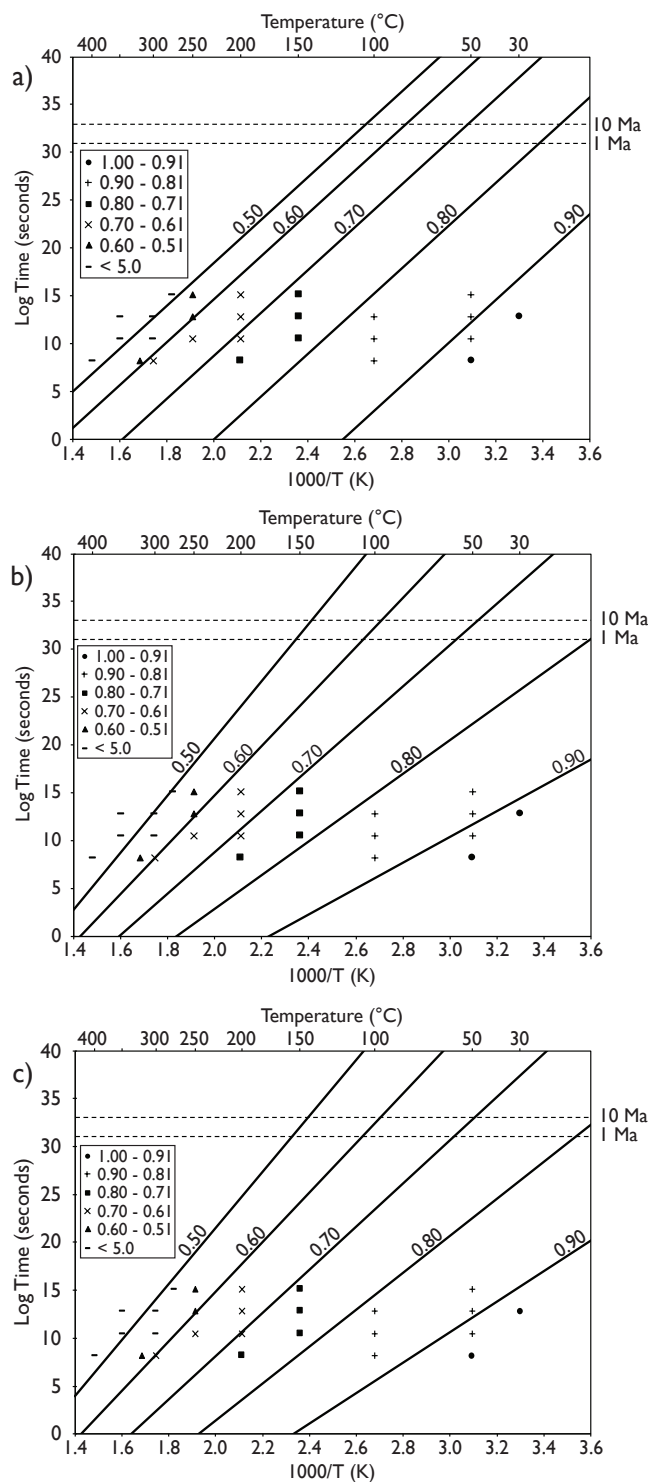
$$465 \quad C_3 = -0.0005542 \pm 0.0003468$$

466

467 Both single and double Box-Cox transforms were applied to Eqs. 10 and 11. A single Box-Cox
468 transformation was better suited to fit the data; however, it did not statistically improve the
469 models. A t-test found that Eq. 11 with a single Box-Cox transformation had a P -value of 0.096.
470 Generally, a P -value < 0.05 suggests strong evidence against the null hypothesis and that it
471 should be rejected. Whereas a p -value > 0.05 indicates weak evidence against the null
472 hypothesis, failing to reject it. In the case of Eq. 11 the null hypothesis is the equation without



473 a transformation and the alternative is to include the single Box-Cox transformation. Using a
474 similar form of test for Eq. 10 found that the C_3 constant produced a p -value of 0.123. This
475 high P -value suggests that the constant is not preferred and that the model from Eq. 11 is
476 more parsimonious. For these reasons, the final fanning models are presented with no
477 transformation (Eq. 10 and 11) and their assumptions can be checked in Figure 9.





479 **Figure 8.** Arrhenius plots with fitted lines extrapolated to geological timescales. (a) parallel model; (b) fanning
 480 model ($T_0 \neq \infty$); and (c) fanning model ($T_0 = \infty$). Each plot was obtained by adopting specific equations: (a) Eq. 3;
 481 (b) Eq. 10; and (c) Eq.11 (see text), and parameters as in Table 4. Values of normalized mean length (r) for each
 482 contour are indicated on the plots, ranging from 0.90 to 0.50. Symbols are the same as for Figure 5.

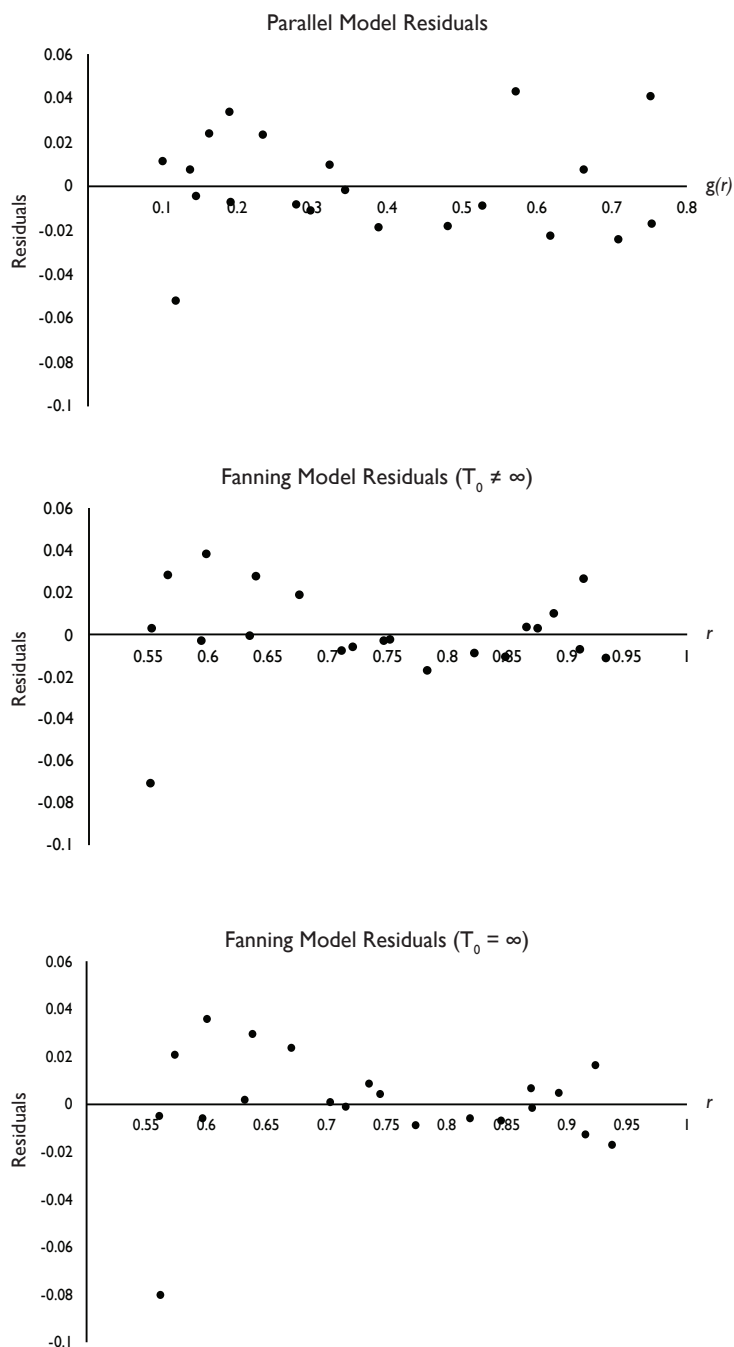
483

484 **Table 4.** Results of the Arrhenius model fitting calculations including estimated temperatures ($^{\circ}\text{C} \pm 2\sigma$ error) for
 485 the monazite partial annealing zone (MPAZ). Note the $T_0 \neq \infty$ estimated MPAZ has no error listed as it is not
 486 possible to reliably calculate the confidence intervals.

	Parallel Model	Fanning Model	
		$T_0 \neq \infty$	$T_0 = \infty$
Model Equation	Eq.3	Eq. 10	Eq. 11
Coefficient of Determination (R^2)	0.99	0.97	0.97
Bottom of MPAZ (2σ) ($^{\circ}\text{C}$)			
Heating Duration:			
1 Ma	-39.64 \pm 6.14	-82.52	-64.30 \pm 13.30
10 Ma	-44.11 \pm 6.49	-89.54	-71.12 \pm 13.78
Top of MPAZ (2σ) ($^{\circ}\text{C}$)			
Heating Duration:			
1 Ma	116.47 \pm 16.06	153.75	157.33 \pm 20.55
10 Ma	101.48 \pm 16.60	140.25	143.26 \pm 21.70

487

488



489
490 **Figure 9.** Residual Plots for the best fitting calculations for each model (ε in Eqs. 3, 10 and 11). Each point
491 represents one annealing experiment.



492

493 **5.3 Comparison of Arrhenius Models**

494 Table 4 and Figure 8 present the results of the model fitting calculations and their associated
495 Arrhenius plots. The models show the full data set with contours of equal length reduction
496 extrapolated to geological timescales. The parallel model, which has a constant activation
497 energy with decreasing r , statistically describes the data slightly better than the two fanning
498 models (coefficient of determination of 0.99 compared to 0.97 for both fanning models).
499 Nevertheless, the two fanning models, which have an increasing activation energy with
500 decreasing r , still describe the data very well. Although the coefficient of determination of the
501 two fanning models are equal, the P -value of 0.128 for constant C_3 in Eq. 10 suggests that the
502 simpler model is the more favourable. Residual plots for each model (Figure 7) show no clear
503 structure suggesting that the residuals do not contradict the linear assumption of the models.
504 In previous studies (e.g. Crowley et al., 1991; Laslett et al., 1987; Yamada et al., 1995), both
505 fanning models have a Box and Cox (1964) or similar type of transformation on the left-hand
506 side of the equation, but because they did not statistically improve them, they were
507 abandoned in this study. The fanning models, as they stand, explain the data very well, and
508 in general, when constructing empirical models to be used as the basis of prediction, simple
509 models with less fitted parameters are generally preferable (Laslett et al., 1987). Regardless
510 of using a transformation or not, all models presented in this study give a statistically
511 satisfactory description of the available data.

512

513 When comparing the models over laboratory timescales, little difference is observed between
514 them, particularly at length reductions < 0.80 . The 0.90 track reduction contour shows the
515 largest difference over laboratory timescales, where both fanning models splay out to lower
516 temperatures. This suggests that fission tracks in monazite are even more sensitive to low
517 temperature annealing in the fanning models compared to the parallel model. As with all such
518 annealing studies, differences in annealing are magnified when the data are extrapolated to
519 geological timescales. The assumption underlying such extrapolations is that track annealing
520 results from the same physical mechanism under both laboratory and geological conditions.
521 All models show that significant reduction in the etchable lengths of fission tracks takes place
522 at ambient and lower temperatures ($< 20^\circ\text{C}$) over geological timescales and that monazite is
523 particularly sensitive to low temperature thermal annealing. Considerably more track



524 shortening would occur in the shallow upper crust between temperatures of ~50 - 160°C over
525 geological timescales of 1 – 10 Ma. Complete annealing of fission tracks occurred very rapidly
526 when the equivalent confined track length reduction decreased below ~0.5.

527

528 Weise et al. (2009) presented a linear fanning model that used contours representing the
529 amount of track length reduction of implanted Kr-tracks in monazite rather than the
530 normalised reduction (l/l_0) as used here. However, similarities can be seen between the
531 different approaches. Both models show considerable track annealing at ambient surface
532 temperatures or below over geological timescales. That is, they are in agreement that a total
533 fission track stability zone is absent for monazite.

534

535 **6. Estimation of the monazite partial annealing zone**

536 Geological temperature ranges for the monazite partial annealing zone (MPAZ) were
537 calculated by extrapolating model equations to the geological timescale with parameters
538 derived from the annealing experiments (Table 4). The lower temperature limit of the MPAZ
539 has been defined as $l/l_0 = 0.95$, since a track length reduction at the 5% level should be clearly
540 detectable under the microscope. The higher temperature limit of the MPAZ is defined at l/l_0
541 = 0.50, which corresponds with the final rapid fading of tracks observed in this study. The
542 parallel model (Figure 8a) shows estimates of the MPAZ for a heating duration of 10^7 years ~-
543 44 – 101°C. Both fanning models estimate a wider temperature range for the same heating
544 duration: -89 – 140°C ($T_0 \neq \infty$); and -71 - 143°C ($T_0 = \infty$). The uncertainties of estimated
545 temperatures are ca. $\pm 6 - 21^\circ\text{C}$ for Eqs. 3 and 11 (2 standard errors). The bootstrapping
546 method for calculating the uncertainties of the estimated MPAZ temperatures could not be
547 confidently calculated for Eq. 10 and therefore error estimates have not been included for
548 this model. The inability to confidently calculate the uncertainties of Eq. 10 further supports
549 the choice of Eq. 11 ($T_0 = \infty$) as the preferred fanning model. Of the two remaining estimates
550 for the MPAZ range (Eqs. 3 and 11), based on the coefficients of determination, the parallel
551 model is slightly preferable. However, the fanning model of Eq. 11 also describes the data
552 almost as well and should not be ruled out. In fact, annealing studies of other minerals such
553 as zircon and apatite have shown a fanning model to best fit their respective datasets (e.g.
554 Ketcham et al., 1999; Laslett et al., 1987; Yamada et al., 1995). Taking the fission track closure



555 temperature (T_c) to be approximately the middle of the MPAZ (Yamada et al., 1995), predicted
556 closure temperatures for the monazite fission track system range between $\sim 45 - 25^\circ\text{C}$ over
557 geological timescales of $10^6 - 10^7$ years. These results are consistent with the findings of
558 Weise et al. (2009), the only other study to estimate a T_c for the monazite fission track system,
559 who estimated T_c to be $< 50^\circ\text{C}$ and perhaps not much above ambient.

560

561 **7. Conclusions**

562 Using implanted ^{252}Cf semi-tracks, isochronal annealing experiments were performed on
563 monazite crystals from the Harcourt Granodiorite in Central Victoria. Semi-track lengths were
564 measured and combined with an estimate of the degree of surface etching to give calculated
565 equivalent confined fission track lengths. The unannealed equivalent confined fission track
566 lengths (control samples) have a mean length of $10.60 \pm 0.19 \mu\text{m}$, which is broadly consistent
567 with the measured lengths of spontaneous ^{238}U confined tracks reported by Weise et al.
568 (2009). As annealing progresses, the mean calculated confined track length decreases
569 anisotropically, with tracks on surfaces perpendicular and parallel to the crystallographic c-
570 axis annealing at measurably different rates.

571

572 Using the equations of Laslett et al. (1987), three empirical models describe the data
573 remarkably well, with the parallel Arrhenius plot fitting the data slightly better than two
574 alternative fanning models. The differences between models are negligible, however, and, in
575 line with experience in other minerals, a fanning model is preferred. Extrapolation of the data
576 to geological timescales suggest that fission tracks in monazite are very sensitive to low
577 temperature annealing and that significant shortening of tracks occurs even at ambient
578 surface temperatures ($\sim 20^\circ\text{C}$) and below. Continued shortening of tracks occurs at
579 temperatures between $\sim 50 - 160^\circ\text{C}$ when extrapolated to geological timescales, with few
580 tracks being recorded at lengths of $l/l_0 < \sim 0.5$. Closure temperatures for fission track retention
581 in monazite are estimated to be only $46 - 25^\circ\text{C}$ over geological timescales of $10^6 - 10^7$ years,
582 consistent with the $< 50^\circ\text{C}$ estimate of Weise et al. (2009).

583

584 As highlighted in Laslett et al. (1987), there is no good reason why the contours in the fanning
585 Arrhenius plot need to be straight and an alternative fanning curvilinear model has been



586 proposed in the case of apatite by Ketcham et al. (2007, 1999). Further experiments to
587 increase the number of data points, especially for even longer heating schedules, would be
588 required to test this model in monazite. Factors that have not been considered in this study
589 and could possibly influence annealing kinetics are compositional effects (e.g. Green et al.,
590 1985), radiation damage effects on etching (e.g. Gleadow, 1981) and radiation enhanced
591 annealing (e.g. McDannell et al. 2019). The validity of this study still requires further
592 confirmation by comparing the predictions from our laboratory results with observations
593 from natural field examples and borehole studies. Nevertheless, it is clear that fission tracks
594 in monazite have the lowest thermal stability of any mineral so far studied and this system
595 has potential for use as an ultra-low temperature thermochronometer.

596

597 ***Author Contributions***

598 SJ is a PhD student who obtained and analysed the presented data as well as prepared the
599 original manuscript. AG and BK provided supervision and contributed to several drafts of the
600 original manuscript. Sample material was provided by AG and BK.

601

602 ***Competing Interests***

603 The authors declare that they have no conflict of interest.

604

605 ***Acknowledgements***

606 We thank Ling Chung for assistance and advice on sample preparation methods and Cameron
607 Patrick from The University of Melbourne Statistical Consulting Centre for assistance with
608 statistical analysis. SJ also acknowledges funding from the Australian Government through an
609 Australian Postgraduate Award (APA). The Melbourne thermochronology laboratory is
610 supported by the AuScope Program funded under the National Collaborative Research
611 Infrastructure Strategy (NCRIS).

612



613 **References**

614

- 615 Badr, M. J., Masoudi, F., Collins, A. S., and Cox, G.: Dating of Precambrian Metasedimentary
616 Rocks and Timing of their Metamorphism in the Soursat Metamorphic Complex (NW
617 IRAN): Using LA-CP-MS , U – Pb Dating of Zircon and Monazite, *Journal of Sciences*,
618 21(4), 311–319, 2010.
- 619 Belton, D. X.: The low-temperature thermochronology of cratonic terranes, Ph.D. thesis,
620 School of Earth Sciences, The University of Melbourne, 2006.
- 621 Box, G. E. P., and Cox, D. R.: An Analysis of Transformations, *J Roy Stat Soc B Met.*, 26(2),
622 211–252, 1964.
- 623 Cenko-Tok, B., Berger, A., and Gueydan, F.: Formation and preservation of biotite - rich
624 microdomains in high - temperature rocks from the Antananarivo Block, Madagascar,
625 *Int J Earth Sci.*, 105(5), 1471–1483, <https://doi.org/10.1007/s00531-015-1265-0>, 2016.
- 626 Clemens, J. D.: Granitic magmas with I-type affinities, from mainly metasedimentary
627 sources: the Harcourt batholith of southeastern Australia, *Contrib Mineral Petr.*,
628 173(11), 1–20, <https://doi.org/10.1007/s00410-018-1520-z>, 2018.
- 629 Crowley, K. d., Cameron, M., and Schaefer, R. I.: Experimental studies of annealing of etched
630 fission tracks in fluorapatite, *Geochim Cosmochim Ac.*, 55(5), 1449–1465,
631 [https://doi.org/10.1016/0016-7037\(91\)90320-5](https://doi.org/10.1016/0016-7037(91)90320-5), 1991.
- 632 Donelick, Raymond A., Roden, M. K., Mooers, J. D., Carpenter, B. S., and Miller, D. S.:
633 Etchable length reduction of induced fission tracks in apatite at room temperature (~
634 23°C): Crystallographic orientation effects and “initial” mean lengths, *International*
635 *Journal of Radiation Applications and Instrumentation. Part, 17(3)*, 261–265.
636 [https://doi.org/10.1016/1359-0189\(90\)90044-X](https://doi.org/10.1016/1359-0189(90)90044-X), 1990.
- 637 Donelick, R. A., O’Sullivan, P. B., and Ketcham, R. A.: Apatite Fission-Track Analysis. *Rev*
638 *Mineral Geochem.*, 58(1), 49–94, <https://doi.org/10.2138/rmg.2005.58.3>, 2005.
- 639 Fayon, A. K.: Fission Track Dating of Monazite: Etching Efficiencies as a Function of U
640 Content, in: *GSA Annual Meeting, Geological Society of America, Minneapolis*, p. 331,
641 2011.
- 642 Fleischer, R. L., Price, P. B., and Walker, R. M.: *Nuclear Tracks in Solids*, Berkeley: University
643 of California Press, 1975.
- 644 Gleadow, A. J. W.: Fission-track dating methods: What are the real alternatives? *Nuclear*



- 645 Tracks, 5, 3–14, [https://doi.org/10.1016/0191-278X\(81\)90021-4](https://doi.org/10.1016/0191-278X(81)90021-4), 1981.
- 646 Gleadow, A. J. W., Raza, A., Kohn, B. P., and Spencer, S. A. S.: The potential of monazite as a
647 new low-temperature fission-track thermochronometer, 10th International Conference
648 on Fission Track Dating, Amsterdam, 2004.
- 649 Gleadow, A. J. W., Gleadow, S. J., Frei, S., Kohlmann, F., and Kohn, B. P.: Automated
650 analytical techniques for fission track thermochronology, *Geochim Cosmochim Acta*,
651 Supplement, 73, A441, 2009.
- 652 Gleadow, A., Kohn, B., & Seiler, C.: The Future of Fission-Track Thermochronology, in:
653 Fission-Track Thermochronology and its Application to Geology, edited by: Malusà, M.
654 and Fitzgerald, P., Springer, 77–92, 2019.
- 655 Green, P. F., Duddy, I. R., Gleadow, A. J. W., Tingate, P. R., and Laslett, G. M.: Fission-track
656 annealing in apatite: Track length measurements and the form of the Arrhenius plot,
657 *Nucl Tracks Rad Meas.*, 10(3), 323–328, [https://doi.org/10.1016/0735-245X\(85\)90121-](https://doi.org/10.1016/0735-245X(85)90121-8)
658 8, 1985.
- 659 Green, P. F., Duddy, I. R., Gleadow, A. J. W., Tingate, P. R., and Laslett, G. M.: Thermal
660 annealing of fission tracks in apatite 1. Variable temperature behaviour, *Chem Geol.:
661 Isotope Geoscience Section*, 59, 237–253, [https://doi.org/10.1016/0168-](https://doi.org/10.1016/0168-9622(88)90019-X)
662 9622(88)90019-X, 1986.
- 663 Hart, S. R.: Diffusion compensation in natural silicates, *Geochim Cosmochim Acta.*, 45, 279–
664 291, 1981.
- 665 Jones, S., Gleadow, A., Kohn, B., and Reddy, S. M.: Etching of fission tracks in monazite: An
666 experimental study, *Terra Nova (Special Issue-Thermo2018)*, 1–10,
667 <https://doi.org/10.1111/ter.12382>, 2019.
- 668 Ketcham, R. A., Donelick, R. A., and Carlson, W. D.: Variability of apatite fission-track
669 annealing kinetics: III. Extrapolation to geological time scales, *Am Mineral.*, 84, 1213–
670 1223, 1999.
- 671 Ketcham, R. A., Carter, A., Donelick, R. A., Barbarand, J. B., and Hurford, A. J.: Improved
672 modeling of fission-track annealing in apatite, *Am Mineral.*, 92(1), 799–810,
673 <https://doi.org/10.2138/am.2007.2281>, 2007.
- 674 Laslett, G. M., Green, P. F., Duddy, I. R., and Gleadow, A. J. W.: Thermal annealing of fission
675 tracks in apatite 2. A quantitative analysis, *Chem Geol.: Isotope Geoscience Section*,
676 65(1), 1–13, [https://doi.org/10.1016/0168-9622\(87\)90057-1](https://doi.org/10.1016/0168-9622(87)90057-1), 1987.



- 677 Malusa, M. G., and Fitzgerald, P. G. (Eds.): Fission-Track Thermochronology and its
678 Application to Geology. Springer Textbooks in Earth Sciences, Geography and
679 Environment, 2019.
- 680 Mcdannell, K. T., Issler, D. R., and Sullivan, P. B. O. :Radiation-enhanced fission track
681 annealing revisited and consequences for apatite thermochronometry, *Geochim*
682 *Cosmochim Ac.*, 252, 213–239, <https://doi.org/10.1016/j.gca.2019.03.006>, 2019.
- 683 Sandhu, A. S., Singh, L., Ramola, R. C., Singh, S., and Virk, H. S.: Annealing Kinetics of Heavy
684 Ion Radiation Damage in Crystalline Minerals, *Nucl Instrum Methods.*, 122–124, 1990.
- 685 Shipley, N. K., and Fayon, A. K. Vanishing Act: Experiments on Fission Track Annealing in
686 Monazite. AGU Fall Meeting Abstracts, 2006.
- 687 Shukoljukov, J. A., and Komarov, A. N.: Tracks of uranium fission in monazite (in Russian),
688 Bulletin of the Commission for the Determination of the Absolute Age of Geological
689 Formations, Moscow: Akad. Nau, USSR, pp. 20–26, 1970.
- 690 Tamer, M., and Ketcham, R.: Is Low-Temperature Fission-Track Annealing in Apatite a
691 Thermally Controlled Process?, *Geochem Geophy Geosy*, 21(3),
692 <https://doi.org/10.1029/2019GC008877>, 2020.
- 693 Tickyj, H., Hartmann, L. A., Vasconcellos, M. A. Z., Philipp, R. P., and Remus, M. V. D.:
694 Electron microprobe dating of monazite substantiates ages of major geological events
695 in the southern Brazilian shield, *J S Am Earth Sci.*, 16, 699–713,
696 <https://doi.org/10.1016/j.jsames.2004.01.001>, 2004.
- 697 Ure, A.: Annealing characteristics of fission tracks in monazite: Application of a new method
698 for performing thermal annealing experiments using implanted ^{252}Cf fission fragment
699 semi-tracks, BSc (Hons) thesis, School of Earth Sciences, The University of Melbourne,
700 2010.
- 701 Wagner, G. A., and Van den Haute, P.: Fission-Track Dating (2nd ed.), Kluwer Academic
702 Publishers, Stuttgart, Germany, 1992.
- 703 Weise, C., van den Boogaart, K. G., Jonckheere, R., and Ratschbacher, L.: Annealing kinetics
704 of Kr-tracks in monazite: Implications for fission-track modelling, *Chem Geol.*, 260(1–2),
705 129–137, <https://doi.org/10.1016/j.chemgeo.2008.12.014>, 2009.
- 706 Yamada, R., Tagami, T., Nishimura, S., and Ito, H.: Annealing kinetics of fission tracks in
707 zircon: an experimental study, *Chem Geol.*, 122(1–4), 249–258,
708 [https://doi.org/10.1016/0009-2541\(95\)00006-8](https://doi.org/10.1016/0009-2541(95)00006-8), 1995.